FULL PAPER

Perovskite Solar Cells

ADVANCED
FUNCTIONAL
MATERIALS

www.afm-journal.de

All-Carbon-Electrode-Based Endurable Flexible Perovskite Solar Cells

Qiang Luo, He Ma, Qinzhi Hou, Yingxiang Li, Jing Ren, Xuezeng Dai, Zhibo Yao, Yu Zhou, Lichen Xiang, Huayun Du, Hongcai He, Ning Wang,* Kaili Jiang,* Hong Lin,* Huaiwu Zhang, and Zhanhu Guo*

Endured, low-cost, and high-performance flexible perovskite solar cells (PSCs) featuring lightweight and mechanical flexibility have attracted tremendous attention for portable power source applications. However, flexible PSCs typically use expensive and fragile indium–tin oxide as transparent anode and high-vacuum processed noble metal as cathode, resulting in dramatic performance degradation after continuous bending or thermal stress. Here, all-carbon-electrode-based flexible PSCs are fabricated employing graphene as transparent anode and carbon nanotubes as cathode. All-carbon-electrode-based flexible devices with and without spiro-OMeTAD (2,2′,7,7′-tetrakis-(*N,N*-di-*p*-methoxyphenylamine)-9,9′-spirobifluorene) hole conductor achieve power conversion efficiencies (PCEs) of 11.9% and 8.4%, respectively. The flexible carbon-electrode-based solar cells demonstrate superior robustness against mechanical deformation in comparison with their counterparts fabricated on flexible indium–tin oxide substrates. Moreover, all carbon-electrode-based flexible PSCs also show significantly enhanced stability compared to the flexible devices with gold and silver cathodes under continuous light soaking or 60 °C thermal stress in air, retaining over 90% of their original PCEs after 1000 h. The promising durability and stability highlight that flexible PSCs are fully compatible with carbon materials and pave the way toward the realization of rollable and low-cost flexible perovskite photovoltaic devices.

1. Introduction

Solution-processed metal halide perovskites are recognized as promising candidates of photoactive materials because of their extraordinary optoelectronic and unique physical properties such as tunable bandgap, strong absorption coefficient, and long carrier diffusion length.[1–4] These intriguing characteristics have allowed for a rapid progress in power conversion efficiency (PCE) of single-junction perovskite solar cells (PSCs), which has been substantially boosted from 3.8% to over 22% due to the continuous efforts on perovskite absorbers, film morphologies, and selective charge contacts.[5–11] One attractive advantage of perovskite materials over the conventional silicon for device fabrication is their low-temperature process capability, which opens the opportunity for the device fabrication on various flexible substrates using low-cost film deposition techniques such as slot-die coating and ink printing.[12,13]

Dr. Q. Luo, Q. Hou, Dr. Y. Li, J. Ren, Prof. H. He, Prof. N. Wang, Prof. H. Zhang
State Key Laboratory of Electronic Thin Film and Integrated Devices
University of Electronic Science and Technology of China
Chengdu 610054, P. R. China
E-mail: wangninguestc@gmail.com

Dr. H. Ma
College of Applied Sciences
Beijing University of Technology
Beijing 100124, P. R. China

Dr. H. Ma, Prof. K. Jiang
State Key Laboratory of Low-Dimensional Quantum Physics
Tsinghua-Foxconn
Nanotechnology Research Center
Department of Physics
Collaborative Innovation
Center of Quantum Matter
Tsinghua University
Beijing 100084, P. R. China
E-mail: JiangKL@mail.tsinghua.edu.cn

The ORCID identification number(s) for the author(s) of this article can be found under https://doi.org/10.1002/adfm.201706777.

X. Dai, Z. Yao, Y. Zhou, Prof. H. Lin
State Key Laboratory of New Ceramics & Fine Processing
School of Material Science and Engineering
Tsinghua University
Beijing 100084, P. R. China
E-mail: hong-lin@mail.tsinghua.edu.cn

Dr. H. Du, Prof. Z. Guo
Integrated Composites Laboratory (ICL)
Department of Chemical & Biomolecular Engineering
University of Tennessee
Knoxville, TN 37996, USA
E-mail: zguo10@utk.edu

Dr. L. Xiang
The Key Laboratory of Material Processing
and Mold of Ministry of Education
Zhengzhou University
Zhengzhou 450001, P. R. China

Prof. N. Wang
State Key Laboratory of Marine Resource Utilization in South China Sea
Hainan University
Haikou 570228, P. R. China

Currently, flexible PSCs have been reported with PCEs in the range of 10–17%.[14–16] Despite the success in obtaining high device efficiencies, the practical application of flexible PSCs is still plagued with several realistic challenges.[15] In high-performance flexible PSCs, indium–tin oxide/polyethylene naphthalate (ITO/PEN) is the popularly used transparent electrode.[12–16] Unfortunately, the scarcity of indium could hinder the advantage of the rapid energy payback of perovskites.[17] Moreover, the poor mechanical robustness of ITO resulted in dramatic performance degradation of flexible PSCs after repeated bending.[18,19] For example, Jung and co-workers have reported an ITO/PEN-based flexible PSC with an initial PCE of 12.2%, while only 50% of PCE was maintained after 1000 cycles with a bending radius of 4 mm.[18] Recently, Ag-mesh/conducting polymer composites have been successfully developed to replace ITO/PEN transparent electrodes for flexible PSCs with enhanced device robustness against mechanical deformation.[19] However, the Ag-mesh/conducting polymer-based flexible PSCs underwent an obvious performance degradation when subjected to thermal stress, decreased by ≈25% after 500 h at 45 °C and ≈77% after 97 h at 70 °C, respectively.[19]

On the other hand, flexible PSCs generally use high-vacuum-processed metals, such as gold and silver, as the preferred back contacts.[14–16] The high price as well as the energy requirements associated with their high vacuum deposition challenges the commercialization of flexible PSCs.[15] In particular, the use of metal electrode limits the long-term stability of PSCs. It was reported recently that the diffusion of metals across the hole transport material (HTM) into the perovskite layer at elevated temperatures caused a dramatic device performance loss.[20–23] This situation is even much worse in inverted PSCs.[24] The metal–electrode-induced performance degradation must be overcome before PSCs can be considered as real products. Although spatially separating the perovskite layer and metal cathode could alleviate the metal–electrode-induced performance degradation to some extent,[23,25] fundamental solution to the cost and stability issues associated with metal cathode in PSCs still relies on developing alternative low-cost and stable back contact materials.

Carbon nanomaterials have shown many advantages over conventional metal oxide transparent electrodes used in solar cells in terms of transparency, cost, stability, and mechanical flexibility.[26] Attempts have been made to apply carbon materials as transparent electrodes in PSCs.[27,28] Very recently, Choi and co-worker applied chemical vapor deposition (CVD)-grown single-layer graphene as transparent electrodes in flexible PSCs and obtained a PCE of 16.8% with superior bending durability,[16] illustrating the advantages of graphene transparent electrodes. In addition, carbon nanomaterials, such as carbon black/graphite composites, carbon nanotubes (CNTs), and graphite, have also been proven to be competitive alternatives to metals as back electrodes in rigid PSCs.[29–32] Compared with other carbon allotropes, CNTs are of special interest for the industry because of their high conductivity, excellent mechanical durability, as well as scalable manufacturing capability. However, integrating CNTs into PSCs with high film quality and conductivity is quite challenging because the fabrication of CNT films from raw CNT powders with aggregated bundles commonly needs the dispersant-aid dispersion and complex film deposition and post-treatment.[33] We have previously designed an advanced and low-cost technique to fabricate free-standing cross-stacking CNT (CSCNT) films from superaligned CNTs array.[34–36] The combinational conductivity and mechanical flexibility of CSCNTs will be an important milestone in the development of low-cost and flexible PSCs.

Considering the attractive features of graphene and CSCNTs, it is promising to simultaneously integrate them into PSCs to create all carbon electrode-based flexible devices. Herein we fabricated, for the first time, a type of all-carbon-electrode flexible PSCs, in which graphene and CSCNTs served as front transparent electrode and back electrode, respectively. All-carbon-electrode-based flexible PSCs, with and without 2,2′,7,7′-tetrakis-(*N*,*N*-di-*p*-methoxyphenylamine)-9,9′-spirobifluorene (spiro-OMeTAD) hole conductor, obtained PCEs of 11.9% and 8.4%, respectively. Furthermore, all-carbon-based flexible PSCs were found to exhibit superior mechanical durability. In addition, flexible PSCs also demonstrated considerably enhanced stability compared with the ITO-based flexible PSCs fabricated with Ag or Au back contacts after continuous light illumination or thermal stress in air, maintaining over 90% of their original PCEs after 1000 h.

2. Results and Discussion

Figure 1a shows the structure of the all-carbon-electrode-based flexible PSC. The flexible device was fabricated on a graphene/PET substrate with a regular device configuration. A compact TiO$_2$ nanocrystalline film was deposited on graphene as electron transport material. [6,6]-phenyl-C61-butyric acid methyl ester (PCBM) was subsequently spin-coated on the top of TiO$_2$ anode to prevent current leakage and to aid in electron extraction. CSCNT film was transferred onto the perovskite layer with the aid of several droplets of diethyl ether. To ensure efficient hole collection, the hole-transporting material of spiro-OMeTAD was cast into the device from CSCNTs' side. Figure 1b shows the energy level of each layer in the device. Figure 1c shows the representative top-surface scanning electron microscopic (SEM) image of graphene/PET film, which is smooth, continuous, transparent, and flexible. The graphene/PET films used in this study also show high transmittance and conductivity, for example, for 2-layered graphene (G2), the sheet resistance and transmittance at the wavelength of 550 nm are ≈290 ± 17 Ω sq^{-1} and 87.3%, respectively, as shown in Figure S1 in the Supporting Information. The as-synthesized TiO$_2$ nanocrystal has an anatase phase (Figure S2, Supporting Information) and a crystal size of ≈ 5 nm as revealed by transmission electron microscopy (TEM) characterization (inset of Figure 1d).[37] Figure 1e shows the representative SEM image of flexible CSCNTs, in which CNT is generally parallel to each other within the same layer and perpendicular to each other between neighboring layers. The perovskite light harvester deposited on graphene/PET substrate showed tetragonal CH$_3$NH$_3$PbI$_3$ characteristic peaks (Figure S3, Supporting Information), as well as crack-free coverage and large crystal size of ≈500 nm (Figure 1f). Figure 1g shows the cross-sectional SEM image of all-carbon-electrode-based flexible PSC. PCBM/TiO$_2$ layer is flat and has an average thickness of 70 nm. The perovskite film is pinhole free with a thickness of about 450 nm, while the CSCNTs have a thickness of about 1.2 μm.
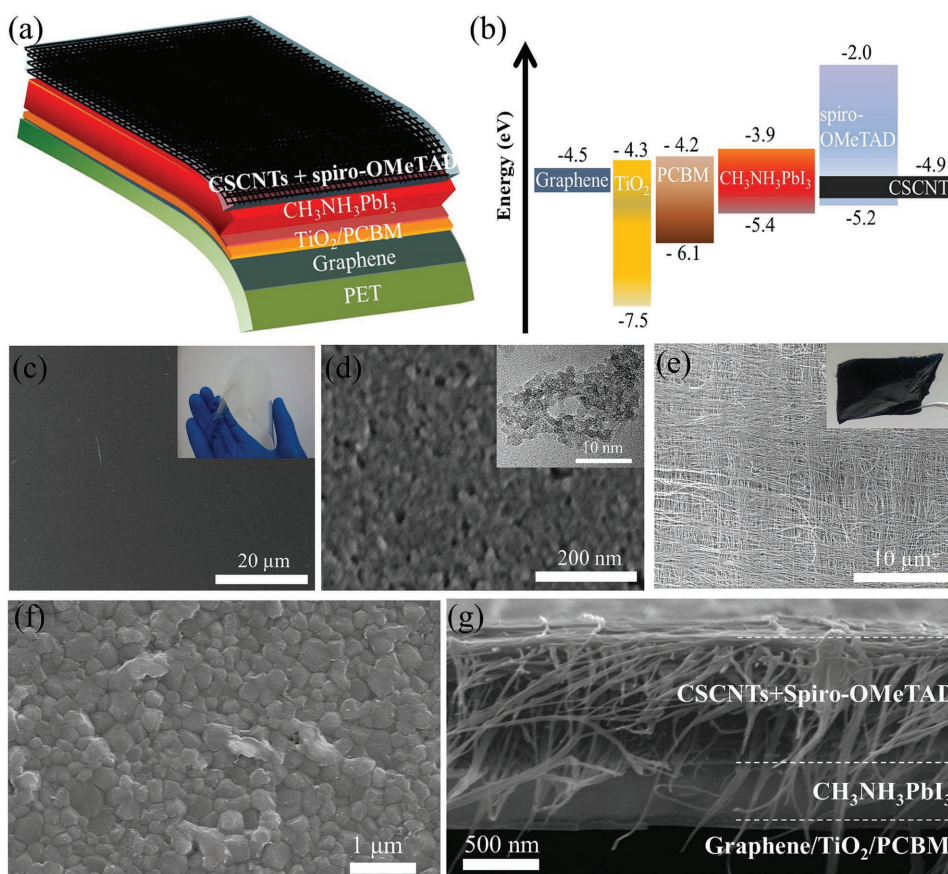
Figure 1. a) Device architecture of the all-carbon-electrode-based flexible PSCs. b) Energy levels of the various device layers in the PSCs. Top view SEM images of c) graphene/PET, d) TiO$_2$, e) CSCNTs, f) perovskite film deposited on TiO$_2$–PCBM/graphene/PET substrate. g) The cross-sectional SEM image of the all-carbon-electrode-based flexible PSCs. Insets in panels (c) and (e) show the photograph of the as-fabricated CSCNTs and graphene/PET, respectively. Inset in panel (d) is the TEM image of the low-temperature prepared TiO$_2$.

Figure 2a shows the photocurrent density versus photovoltage (J–V) curves of the best-performing all-carbon-based flexible PSCs with different graphene electrodes. For simplicity, the electrodes with 1, 2, and 3-layered graphene are abbreviated as G1, G2, and G3, respectively. The key photovoltaic parameters including the short-circuit photocurrent density (J_{sc}), open-circuit photovoltage (V_{oc}), and fill factor (FF) are listed in Table S1 (Supporting Information). Flexible PSC fabricated with G1 electrode showed a J_{sc} of 20.8 mA cm^{-2}, V_{oc} of 0.88 V, FF of 0.52, and PCE of 9.6%. The PCE of the flexible PSC incorporating the G2 electrode can be increased to 11.9% due to the enhanced FF (0.65). The improved FF and PCE can be attributed to the decreased sheet resistance and enhanced electron extraction. As indicated by the time-resolved photoluminescence (TRPL) spectra using bi-exponential function fitting (Figure S4 and Table S2, Supporting Information), the G1-based perovskite film exhibited a decay time up to $\tau_1 = 0.91$ ns and $\tau_2 = 8.42$ ns (τ_1 is attributed to the charge extraction across the interface between perovskite and electron transport layer, and τ_2 originates from the radiative recombination[38,39]). For G2-loaded
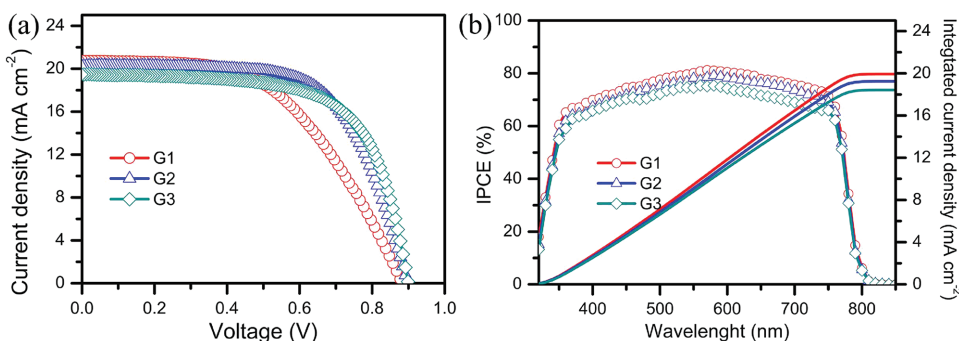
Figure 2. a) J–V curves and b) IPCE spectra of the all-carbon-electrode-based flexible PSCs fabricated with different graphene/PET transparent electrodes.
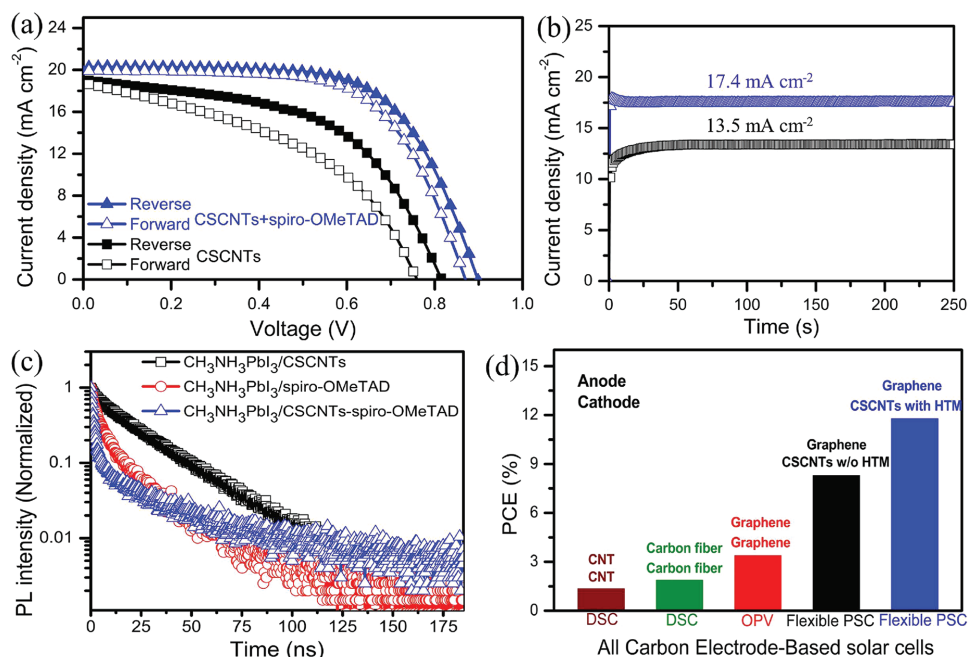
Figure 3. a) J–V curves of the all-carbon-electrode-based flexible PSCs with or without spiro-OMeTAD hole conductor under forward (from −0.1 to 1.2 V) and reverse (from 1.2 to −0.1 V) scans. b) The stabilized photocurrent densities measured under constant bias of 0.66 V (with spiro-OMeTAD) and 0.57 V (without spiro-OMeTAD). c) Time-resolved photoluminescence spectra of $CH_3NH_3PbI_3$ perovskite interfaced with different charge contacts. d) PCEs of different all-carbon-electrode-based solar cells, including all-carbon solar cells,[19] dye-sensitized solar cells (DSCs),[20] organic solar cells (OPVs),[21] and flexible PSCs in this work.

perovskite, τ_1 and τ_2 were shortened to 0.52 and 6.34 ns, respectively, and τ_2 was almost overwhelmed by τ_1 (the relative amplitude is 99%), suggesting that the decreased sheet resistance also contributed to the enhanced electron extraction. In the case of G3 device, although the FF can be further increased to 0.67, J_{sc} is decreased to 19.3 mA cm^{-2}, leading to a slightly lower PCE. The decreased J_{sc} can be ascribed to the fact that more layers of graphene imply a lower transmittance.[27] Therefore, the optimum PCE of the as-fabricated flexible PSCs is a compromise between the conductivity and the transmittance of the graphene electrode. Integrating the incident photon to current efficiency (IPCE) spectra, Figure 2b, yielded photocurrent densities of 19.9, 19.2, and 18.4 mA cm^{-2} for the flexible PSCs fabricated with G1, G2, and G3 electrodes, respectively, which were consistent (less than 6% deviation) with the measured J_{sc} from the scanned J–V curves. Impedance spectroscopy was used to clarify the charge recombination behaviors. Only one semicircle arc was observed in the Nyquist plots in dark (Figure S5, Supporting Information), which could be attributed to the overall recombination resistance (R_{rec}).[40,41] It is found that the R_s (series resistance) among these three devices is in the order of $R_s(G3) < R_s(G2) < R_s(G1)$, and the R_{rec} values for the G2- and G3-based solar cells were significantly higher than that of G1-based device, indicating a lower recombination rate in the G2- and G3-based devices.

Figure 3a presents the J–V curves of G2-based solar cells fabricated with or without additional spiro-OMeTAD hole transport conductor. The extracted photovoltaic parameters are summarized in Table S3 (Supporting Information). The G2-based flexible PSCs with spiro-OMeTAD show negligible J–V hysteresis, with the PCEs of 11.9% and 11.1% measured

under reverse and forward scans, respectively. Encouragingly, the hole-conductor-free flexible PSC also achieved promising PCEs of 8.4% and 6.4% measured under reverse and forward scans, respectively. To the best of our knowledge, this is also the first demonstration on the hole-conductor-free carbon back electrode-based flexible PSCs. The photocurrent densities of the flexible PSCs near their maximum power points were stabilized to 17.4 and 13.5 mA cm^{-2} (Figure 3b), yielding stabilized PCEs of 11.4% and 7.7% for the flexible devices with or without spiro-OMeTAD, respectively. Moreover, the incorporation of the spiro-OMeTAD hole conductor also increased the average efficiency of the flexible PSCs (10.2 ± 1.2% vs 7.1 ± 1.3%, Figure S6, Supporting Information). To elucidate the effect of spiro-OMeTAD on the device performance, the charge-carrier dynamics in pristine and CSCNT-containing perovskite films were investigated using a steady-state PL measurement. For comparison, the sample of pristine perovskite interfaced with spiro-OMeTAD was also examined. The steady-state PL result is shown in Figure S7 (Supporting Information). The pristine perovskite film shows an intense PL emission peak at around 770 nm. In the presence of a charge-extraction layer (CSCNTs, spiro-OMeTAD, or CSCNT–spiro-OMeTAD), the PL of the pristine perovskite film was strongly quenched, indicating a rapid extraction of charges across the interfaces after photon excitation. TRPL spectroscopy was further used to evaluate the charge-carrier dynamics quantitatively, as shown in Figure 3c. The pristine perovskite film exhibited a long charge-carrier lifetime of τ_{10} = 185 ns (Figure S8 in the Supporting Information, τ_{10} is the time at which the initial PL intensity decreases by a factor of 10[42,43]). In comparison, the charge-carrier lifetime

of perovskite films decreased obviously when interfaced with CSCNT (τ_{10} = 46 ns), and spiro-OMeTAD (τ_{10} = 17 ns). Moreover, the charge transfer from the perovskite to the CSCNT–spiro-OMeTAD (τ_{10} = 6 ns) was more rapid than that from perovskite to that of CSCNT or spiro-OMeTAD, indicating that the CSCNT and spiro-OMeTAD can synergistically facilitate the charge extraction and transportation. The sufficient hole extraction and transportation could considerably hinder the negative ionic charge accumulation at the $CH_3NH_3PbI_3$/charge contact interfaces, which ultimately resulted in higher PCEs and negligible J–V hysteresis in the CSCNT–spiro-OMeTAD-based flexible PSCs.[44,45] In addition, it is worth noting that in this study all-carbon-electrode-based flexible PSCs (with or without spiro-OMeTAD) also demonstrated higher PCEs compared with other kinds of all-carbon-electrode-based solar cells (Figure 3d), including all-carbon-solar cells ($\approx 5.7 \times 10^{-3}$%),[46] all-carbon-fiber-electrode-based dye-sensitized solar cells (<2%),[47,48] and all graphene-electrode-based organic solar cells (3.4%).[49]

The mechanical flexibility of all-carbon-electrode-based flexible PSCs was evaluated by bending at different bending curvature and bending cycles. First, the bending test was performed with different curvature radii, from 8 to 2.2 mm under 200 bending cycles (**Figure 4**a). For comparison, reference ITO-based flexible PSCs with the standard structure of PEN/ITO/TiO_2/PCBM/$CH_3NH_3PbI_3$/spiro-OMeTAD/Au (ITO/Au) were also fabricated. The PCE of carbon-based flexible PSCs had almost no decrease even after bending with 4 mm curvature and then slightly decreased to 85% of

the original efficiency at a curvature radius of 2.2 mm. In contrast, the PCE of ITO-based solar cell suffered an obvious reduction to 87% when curvature was lowered to 4 mm and a further bending to 2.2 mm almost led to the complete damage of the device. Next, the bending curvature was fixed to 4 mm, and multiple bending cycles were conducted. All-carbon-electrode-based PSC was found to keep about 84% of its original value after 2000 bending cycles, which mainly originated from the reduced J_{sc} (11% loss) and FF (6% loss), as shown in Figure S9 (Supporting Information). However, the FF and J_{sc} of the ITO-based flexible PSC were decreased by 67% and 41%, respectively, leading to the device efficiency decreased to 13% of its initial value after 1500 bending cycles. To find out the origin of performance degradation, the electrical resistance changes ($\triangle R/R_0$(%)) of 2-layered graphene/PET, CSCNTs, and ITO/PEN electrodes were examined as a function of the bending cycle at the curvature radius of 4 mm, as shown in Figure S10 (Supporting Information). The resistance of ITO/PEN is dramatically increased after continuous bending, indicating that the performance degradation of the ITO/PEN-based flexible PSCs largely originated from the conductivity loss in the brittle ITO layer.[18,19] However, the efficiency of the all-carbon-electrode-based flexible PSCs is still degraded by 16% after 2000 bending cycles although the resistance of CSCNT and graphene electrodes is unchanged, most likely due to the fracture generated in crystalline perovskite layer and delamination in the devices under deformation.[14]
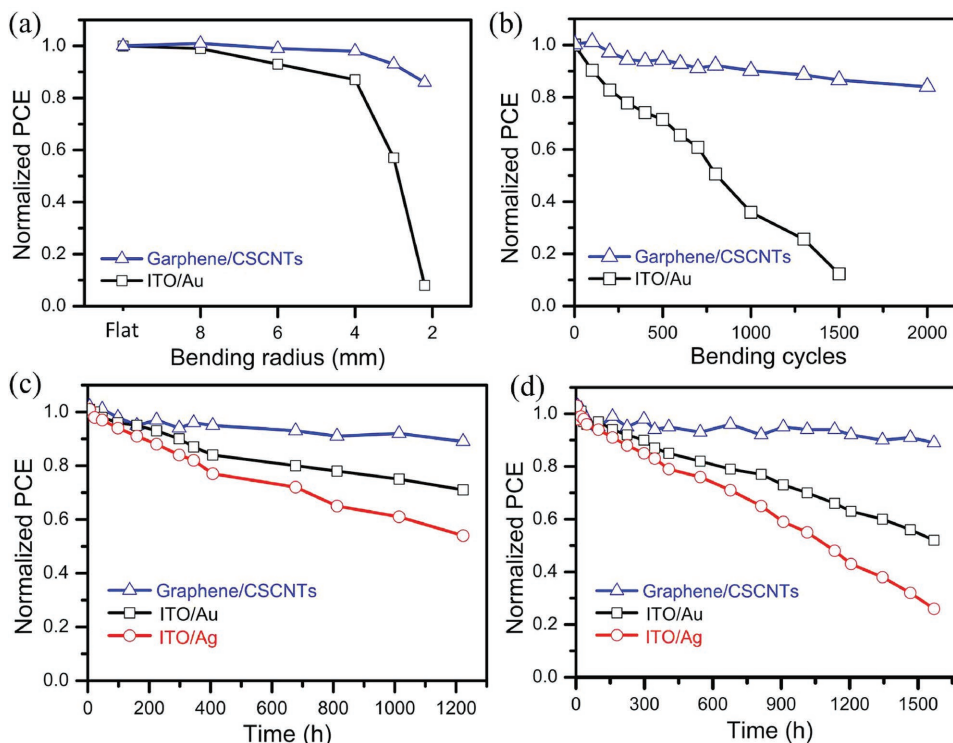
Figure 4. a) PCE evolution of the flexible devices upon increasing bending curvature radius after 200 bending cycles. b) Bending durability of the ITO/PEN-based and all-carbon-electrode-based flexible solar cells as a function of bending cycles. c) Efficiency stability of the standard and all-carbon-electrode-based flexible PSCs as a function of soaking time in different conditions c) in ambient atmosphere under AM 1.5G illumination in air without UV filter, and d) in ambient atmosphere with constant heating temperature of 60 °C.

**ADVANCED
SCIENCE NEWS**
www.advancedsciencenews.com

**ADVANCED
FUNCTIONAL
MATERIALS**
www.afm-journal.de

The commercial viability of flexible PSCs is strongly related to their long-term stability when subjected to real working conditions. In particular, solar cells are normally operated under light soaking and elevated temperatures. The photostability of the as-fabricated flexible PSCs was first examined under AM 1.5G irradiation in air (average temperature 19 ± 3 °C, average relative humidity 38 ± 6%). For comparison, the photostability of the ITO/PEN-based flexible PSCs with Au (ITO/Au) or Ag (ITO/Ag) as back electrodes was also examined. The corresponding J–V curves of the control ITO-based solar cells is shown in Figure S11 (Supporting Information). As shown in Figure 4c, the all-carbon-electrode-based PSCs remained 92% of their original value after 1014 h light soaking, outperforming the reference Au-based (≈75%) and Ag-based flexible solar cells (≈61%). The thermal stability of the as-fabricated G2-based flexible PSCs was also evaluated by subjecting the devices to a constant temperature in air. As shown in Figure 4d, when subjected to a continuous thermal treatment at 60 °C in dark and in air, the PCEs were degraded to 26% and 52% of their initial values for Ag- and Au-based reference devices, respectively, which could be ascribed to the irreversible changes caused by the diffusion of metals into the perovskite layer and the accelerated moisture ingress at elevated temperatures.[23,50] In sharp contrast, all-carbon-electrode flexible PSCs exhibited considerably enhanced performance preservation, remaining about 89% of the initial PCE after 1570 h, which is also significantly better than that of flexible PSCs using Ag-mesh/conducting polymer as transparent electrodes (decreased to ≈75% after 500 h at 45 °C and ≈23% after 97 h at 70 °C).[19] The enhanced thermal stability of carbon-based solar cells in humid air can be ascribed to two aspects. First, the carbon electrode layer exerted a little effect on the perovskite underlayer. Second, the thick and hydrophobic CSCNT layer (≈1.2 µm) combined with spiro-OMeTAD provided a stable encapsulating layer to protect perovskite from moisture aggression. To confirm the latter case, the humidity stability of perovskite films in CSCNT–spiro-OMeTAD- and Au–spiro-OMeTAD-based solar cells (substrate: graphene/PET) was examined by X-ray diffraction (XRD) characterization to determine if CSCNT–spiro-OMeTAD provided an enhanced protection of perovskite from moisture ingress. To enable the characterization of the actually degraded perovskite films in flexible PSCs, CSCNT–spiro-OMeTAD- and Au–spiro-OMeTAD-based solar cells were first subjected to a high humidity of 70% in dark for 300 h, after which CSCNT–spiro-OMeTAD and Au–spiro-OMeTAD were peeled off using scotch tape and the remaining spiro-OMeTAD was subsequently removed via the immersion of perovskite film into chlorobenzene solvent.[51] The detailed experiment procedure can be found in the "Experimental Section." As observed in Figure S12 (Supporting Information), after 300 h of exposure, the most obvious change of perovskite film in Au-electrode-based solar cells was the appearance of a strong PbI_2 peak of (001) face at 12.5°, indicating that the $CH_3NH_3PbI_3$ perovskite experienced a severe degradation in Au-electrode-based solar cells in a constant humidity of 70%. In the case of perovskite film in the CSCNT–spiro-OMeTAD-based devices, no discernible PbI_2 peak was observed after 300 h of exposure, indicating that the thick CSCNT–spiro-OMeTAD layer provided an enhanced protection of perovskite from moisture ingress.

Therefore, the hydrophobic surface of CSCNT, as well as the thick CSCNT–spiro-OMeTAD layer, synergically inhibited the moisture ingress, leading to the enhanced light soaking or thermal stress stability in humid air.

3. Conclusion

In summary, for the first time, all-carbon-electrode-based flexible PSCs were fabricated with graphene as the front transparent anode and carbon nanotubes as the back electrode. By using low-temperature synthesized TiO_2 combined with PCBM as electron extracting material, then all-carbon-electrode-based flexible PSCs fabricated with and without spiro-OMeTAD hole conductor showed PCEs of 11.9% and 8.4%, respectively. The carbon-based flexible PSCs obtain 86% of the original PCEs even after 2000 bending cycles at a curvature radius of 4 mm, significantly outperforming the conventional flexible PSCs fabricated with ITO/PEN transparent electrode and metal back electrode. Moreover, the all-carbon-electrode-based flexible PSCs exhibited good performance preservation, retaining over 90% of their original efficiencies after 1000 h light soaking or thermal stress in humid air. Considering the increasing efforts dedicated to developing low-cost and efficient flexible energy conversion devices, the promising efficiency, flexibility, and long-term stability of all-carbon-electrode-based flexible PSCs clearly demonstrate the sufficient compatibility of carbon materials with flexible PSCs and highlight the potential of incorporating alternative electrode materials in achieving high efficiency, endurable, and large-scale perovskite photovoltaic devices.

4. Experimental Section

Materials: Graphene transparent electrodes were purchased from 2D Carbon (Changzhou) Tech. Inc., LTD, China, which were prepared by transferring CVD synthesized graphene onto the PET substrates. Perovskite precursor was prepared by dissolving lab-synthesized methylammonium iodide (CH_3NH_3I)[8] and PbI_2 into dimethyl sulfoxide/N,N-dimethyl formamide (3:7, volume ratio). The total mass concentration of perovskite precursor was 40 wt%.

Preparation of TiO_2 Nanocrystal: TiO_2 was synthesized by a low-temperature nonaqueous route.[37] Briefly, 1 mL of $TiCl_4$ solution was slowly added to 4 mL of ethanol under stirring; then 20 mL of anhydrous benzyl alcohol was added to the mixture solution. After vigorous stirring for 30 min, the solution was heated to 80 °C for a period of 8 h. After cooling down naturally to ambient temperature, 2 mL of the resulting suspension was slowly added to 18 mL of diethyl ether. The as-obtained precipitation was centrifuged at 5000 rpm and washed with acetone. Then TiO_2 was redispersed in ethanol by sonication (2 wt%). To enhance the adhesive properties of TiO_2 nanoparticles, a small amount of titanium di-isopropoxide bis(acetylacetonate) was added to the colloidal TiO_2 dispersion.

Fabrication of CSCNT: Highly superaligned CNT arrays (length: ≈300 µm) were first prepared on silicon wafers by chemical vapor deposition using iron as the catalyst and acetylene as the precursor according to the previous method.[34,35] The substrate was placed in the tube furnaces and then heated up to 680–720 °C in the flowing argon gas for 15 min. Subsequently, hydrogen and acetylene were injected into reaction system. Superaligned arrays can be obtained under the conditions of 500 sccm acetylene plus 50 sccm hydrogen. CSCNT films were fabricated by cross-stacking the superaligned CNT arrays on a metallic frame.[36] The CSCNT films were shrunk and tightened by

dipping them into ethanol for 10 s. The CSCNT electrode exhibited a sheet resistance of $41 \pm 1.8\ \Omega\ \mathrm{sq}^{-1}$.

Device Fabrication: TiO_2 nanocrystal was deposited on the graphene substrates by spin-coating at 5000 rpm, and then drying at 45 °C in vacuum. PCBM with an optimized concentration of 15 mg mL^{-1} was then spin-coated onto the TiO_2 layer (5000 rpm). Subsequently, in an N_2-purged glovebox, the perovskite precursor solution was spin-coated onto the TiO_2/PCBM layer by two consecutive spin-coating steps of 1000 and 4000 rpm for 10 and 45 s, respectively. About 500 µL ethyl acetate was rapidly dropped on the perovskite films after 30 s of spin-coating. The films were heated in a vacuum-drying cabinet at 50 °C for 4 h. CSCNT films were then transferred onto perovskite layer with the aid of several droplets of chlorobenzene. HTM was incorporated from CSCNTs' side. HTM solution was prepared by adding 72.3 mg of spiro-OMeTAD, 28.8 µL of 4-tert-butylpyridine, and 17.5 µL of lithium bis(trifluoromethylsulfonyl)imide (520 mg mL^{-1} in acetonitrile) to 1 mL of chlorobenzene. The fabricated devices were remained in drying air for 48 h before test.

Standard flexible solar cells were fabricated by replacing the graphene electrodes with ITO/PEN electrodes. The fabrication process of TiO_2/PCBM and perovskite layers on ITO/PEN substrates was similar to the carbon electrode-based devices. Au or Ag electrode was deposited onto the HTM layer by thermal evaporation.

Characterization: The XRD pattern of TiO_2 nanocrystal was recorded on a Bruker D8 Advance diffractometer with Cu Kα1 radiation. The morphologies of samples were characterized with SEM (LEO 1530, Gemini, Zeiss, Germany). The photocurrent–photovoltage (*J–V*) curves of solar cells were collected by using a digital source meter (2401, Keithley Instruments, USA) under AM 1.5G irradiation (100 mW cm^{-2}). A standard silicon-based solar cell was used to calibrate the intensity of light source. The *J–V* curves for all devices were measured by masking the active area with a metal mask ($0.15\ \mathrm{cm}^2$). IPCE spectra were recorded using a quantum efficiency measurement system (QEX10, PV measurements, USA). Impedance spectroscopy was characterized by using a Zahner system (Zahner, Zahner-Electrik GmbH& Co., KG, Germany) in the frequency range from 2 MHz to 1 Hz, which was recorded at 0.6 V in dark. To realize the XRD characterization of the actually degraded perovskite films in the flexible PSCs, CSCNT–spiro-OMeTAD- and Au–spiro-OMeTAD-based solar cells were fabricated. The Au–spiro-OMeTAD-based devices were also fabricated on graphene/PET. Before characterization, solar cells were first exposed to a constant humidity of 70% and a temperature of 25 °C in dark for 300 h. The humidity and temperature were controlled by using a temperature–humidity chamber (RP-80A, Beijing Hongzhan Instrument Co., Ltd.). After that, CSCNT–spiro-OMeTAD and Au layers were peeled off using Kapton tape, then the films were immersed into chlorobenzene solvent to selectively remove the remaining spiro-OMeTAD. After 30 s, the films were removed from the chlorobenzene solution and were dried under an N_2 stream. Those successive steps can selectively remove the CSCNTs, Au electrode, and spiro-OMeTAD hole transport material without destroying the perovskite light absorber.

Supporting Information

Supporting Information is available from the Wiley Online Library or from the author.

Acknowledgements

Conflict of Interest

The authors declare no conflict of interest.

Keywords

[1] C. Wehrenfennig, G. E. Eperon, M. B. Johnston, H. J. Snaith, L. M. Herz, *Adv. Mater.* **2014**, *26*, 1584.

[2] M. A. Green, A. Ho-Baillie, H. J. Snaith, *Nat. Photonics* **2014**, *8*, 506.

[3] D. Amgar, S. Aharon, L. Etgar, *Adv. Funct. Mater.* **2016**, *26*, 8576.

[4] Q. Dong, Y. Fang, Y. Shao, P. Mulligan, J. Qiu, L. Cao, J. Huang, *Science* **2015**, *347*, 6225.

[5] A. Kojima, K. Teshima, Y. Shirai, T. Miyasaka, *J. Am. Chem. Soc.* **2009**, *131*, 6050.

[6] H. S. Kim, C. R. Lee, J. H. Im, K. B. Lee, T. Moehl, A. Marchioro, S. J. Moon, R. Humphry-Baker, J. H. Yum, J. E. Moser, M. Grätzel, N. G. Park, *Sci. Rep.* **2012**, *2*, 591.

[7] M. M. Lee, J. Teuscher, T. Miyasaka, T. N. Murakami, H. J. Snaith, *Science* **2012**, *338*, 643.

[8] J. Burschka, N. Pellet, S. J. Moon, R. Humphry-Baker, P. Gao, M. K. Nazeeruddin, M. Gratzel, *Nature* **2013**, *499*, 316.

[9] N. J. Jeon, J. H. Noh, W. S. Yang, Y. C. Kim, S. Ryu, J. Seo, S. I. Seok, *Nature* **2015**, *517*, 476.

[10] M. Saliba, T. Matsui, K. Domanski, J. Y. Seo, A. Ummadisingu, S. M. Zakeeruddin, J. P. Correa-Baena, W. R. Tress, A. Abate, A. Hagfeldt, M. Grätzel, *Science* **2016**, *354*, 206.

[11] W. S. Yang, B. W. Park, E. H. Jung, N. J. Jeon, Y. C. Kim, D. U. Lee, S. S. Shin, J. Seo, E. K. Kim, J. H. Noh, S. I. Seok, *Science* **2017**, *356*, 1376.

[12] J. You, Z. Hong, Y. Yang, Q. Chen, M. Cai, T. Song, C. Chen, S. Lu, Y. Liu, H. Zhou, Y. Yang, *ACS Nano* **2014**, *8*, 1674.

[13] M. Kaltenbrunner, G. Adam, E. D. Glowacki, M. Drack, R. Schwodiauer, L. Leonat, D. H. Apaydin, H. Groiss, M. C. Scharber, M. S. White, N. S. Sariciftci, S. Bauer, *Nat. Mater.* **2015**, *14*, 1032.

[14] M. M. Tavakoli, K. H. Tsui, Q. Zhang, J. He, Y. Yao, D. Li, Z. Fan, *ACS Nano* **2015**, *9*, 10287.

[15] F. D. Giacomo, A. Fakharuddin, R. Jose, T. M. Brown, *Energy Environ. Sci.* **2016**, *9*, 3007.

[16] J. Yoon, H. Sung, G. Lee, W. Cho, N. Ahn, H. S. Jung, M. Choi, *Energy Environ. Sci.* **2017**, *10*, 337.

[17] W. Guo, Z. Xu, F. Zhang, S. Xie, H. Xu, X. Liu, *Adv. Funct. Mater.* **2016**, *26*, 8855.

[18] B. J. Kim, D. H. Kim, Y. Y. Lee, H. W. Shin, G. S. Han, J. S. Hong, K. Mahmood, T. K. Ahn, Y. C. Joo, K. S. Hong, N. G. Park, S. Lee, H. S. Jung, *Energy Environ. Sci.* **2015**, *8*, 916.

[19] Y. Li, L. Meng, Y. Yang, G. Xu, Z. Hong, Q. Chen, J. You, G. Li, Y. Yang, Y. Li, *Nat. Commun.* **2016**, *7*, 10214.

[20] Y. Han, S. Meyer, Y. Dkhissi, K. Weber, J. M. Pringle, U. Bach, L. Spiccia, Y. B. Cheng, *J. Mater. Chem. A* **2015**, *3*, 8139.

[21] S. Cacovich, L. Cina, F. Matteocci, G. Divitini, P. A. Midgley, A. Di Carlo, C. Ducati, *Nanoscale* **2017**, *9*, 4700.

[22] Y. Kato, L. K. Ono, M. V. Lee, S. Wang, S. R. Raga, Y. Qi, *Adv. Mater. Interfaces* **2015**, *2*, 1500195.

[23] K. Domanski, J. P. Correa-Baena, N. Mine, M. K. Nazeeruddin, A. Abate, M. Saliba, W. Tress, A. Hagfeldt, M. Grätzel, *ACS Nano* **2016**, *10*, 6306.

**ADVANCED
SCIENCE NEWS**

www.advancedsciencenews.com

**ADVANCED
FUNCTIONAL
MATERIALS**

www.afm-journal.de

[24] J. Li, Q. Dong, N. Li, L. Wang, *Adv. Energy Mater.* **2017**, *7*, 1602922.

[25] W. Chen, Y. Wu, Y. Yue, J. Liu, W. Zhang, X. Yang, H. Chen, E. Bi, I. Ashraful, M. Grätzel, L. Han, *Science* **2015**, *350*, 944.

[26] J. Du, S. Pei, L. Ma, M. Cheng, *Adv. Mater.* **2014**, *26*, 1958.

[27] P. You, Z. Liu, Q. Tai, S. Liu, F. Yan, *Adv. Mater.* **2015**, *27*, 3632.

[28] Z. Liu, P. You, C. Xie, G. Tang, F. Yan, *Nano Energy* **2016**, *28*, 151.

[29] A. Mei, X. Li, L. Liu, Z. Ku, T. Liu, Y. Rong, M. Xu, M. Hu, J. Chen, Y. Yang, M. Grätzel, H. Han, *Science* **2014**, *345*, 295.

[30] Z. Wei, K. Yan, H. Chen, Y. Yi, T. Zhang, X. Long, J. Li, L. Zhang, J. Wang, S. Yang, *Energy Environ. Sci.* **2014**, *7*, 3326.

[31] Q. Luo, H. Ma, Y. Zhang, X. Yin, Z. Yao, N. Wang, J. Li, S. Fan, K. Jiang, H. Lin, *J. Mater. Chem. A* **2016**, *4*, 5569.

[32] Z. Wei, H. Chen, K. Yan, X. Zheng, S. Yang, *J. Mater. Chem. A* **2015**, *3*, 24226.

[33] L. Yu, C. Shearer, J. Shapter, *Chem. Rev.* **2016**, *116*, 13413.

[34] K. Jiang, Q. Li, S. Fan, *Nature* **2002**, *419*, 801.

[35] X. Zhang, K. Jiang, C. Feng, P. Liu, L. Zhang, J. Kong, T. Zhang, Q. Li, S. Fan, *Adv. Mater.* **2006**, *18*, 1505.

[36] K. Liu, Y. Sun, P. Liu, X. Lin, S. Fan, K. Jiang, *Adv. Funct. Mater.* **2011**, *21*, 2721.

[37] K. Wojciechowski, M. Saliba, T. Leijtens, A. Abate, H. J. Snaith, *Energy Environ. Sci.* **2014**, *7*, 1142.

[38] Y. Li, Y. Zhao, Q. Chen, Y. Yang, Y. Liu, Z. Hong, Z. Liu, Y. T. Hsieh, L. Meng, Y. Li, Y. Yang, *J. Am. Chem. Soc.* **2015**, *137*, 15540.

[39] L. Zhao, D. Luo, J. Wu, Q. Hu, W. Zhang, K. Chen, T. Liu, Y. Liu, Y. Zhang, F. Liu, T. Russel, H. Snaith, R. Zhu, Q. Gong, *Adv. Funct. Mater.* **2016**, *26*, 3508.

[40] L. Liu, A. Mei, T. Liu, P. Jiang, Y. Sheng, L. Zhang, H. Han, *J. Am. Chem. Soc.* **2015**, *137*, 1790.

[41] Q. Luo, H. Chen, Y. Lin, H. Du, Q. Hou, F. Hao, N. Wang, Z. Guo, J. Huang, *Adv. Funct. Mater.* **2017**, *27*, 1702090.

[42] L. Kong, G. Liu, J. Gong, Q. Hu, R. D. Schaller, P. Dera, D. Zhang, Z. Liu, W. Yang, K. Zhu, Y. Tang, C. Wang, S. Wei, T. Xu, H. Mao, *Proc. Natl. Acad. Sci. USA* **2016**, *113*, 8910.

[43] N. Arora, M. L. Dar, A. Hinderhofer, N. Pellet, F. Schreiber, S. M. Zakeeruddin, M. Graetzel, *Science* **2017**, *358*, 768, https://doi.org/10.1126/science.aam5655.

[44] B. Wu, K. Fu, N. Yantara, G. Xing, S. Sun, T. C. Sum, N. Mathews, *Adv. Energy Mater.* **2015**, *5*, 1500829.

[45] S. Meloni, T. Moehl, W. Tress, M. Franckevičius, M. Saliba, Y. H. Lee, P. Gao, M. K. Nazeeruddin, S. M. Zakeeruddin, U. Rothlisberger, M. Graetzel, *Nat. Commun.* **2016**, *7*, 10334.

[46] M. P. Ramuz, M. Vosgueritchian, P. Wei, C. Wang, Y. Gao, Y. Wu, Y. Chen, Z. Bao, *ACS Nano* **2012**, *6*, 10384.

[47] A. K. K. Kyaw, H. Tantang, T. Wu, L. Ke, J. Wei, H. V. Demir, Q. Zhang, X. W. Sun, *J. Phys. D: Appl. Phys.* **2012**, *45*, 165103.

[48] X. Cai, S. Hou, H. Wu, Z. Lv, Y. Fu, D. Wang, C. Zhang, H. Kafafy, Z. Chu, D. Zou, *Phys. Chem. Chem. Phys.* **2012**, *14*, 125.

[49] Z. Liu, P. You, S. Liu, F. Yan, *ACS Nano* **2015**, *9*, 12026.

[50] J. Zhao, X. Zheng, Y. Deng, T. Li, Y. Shao, A. Gruverman, J. Shield, J. Huang, *Energy Environ. Sci.* **2016**, *9*, 3650.

[51] J. M. Kadro, N. Pellet, F. Giordano, A. Ulianov, O. Muntener, J. Maier, M. Gratzel, A. Hagfeldt, *Energy Environ. Sci.* **2016**, *9*, 3179.